Applied Energy 157 (2015) 729–743

Contents lists available at ScienceDirect

Applied Energy

journal homepage: www.elsevier.com/locate/apenergy

Design methodology for radial turbo expanders in mobile organic Rankine cycle applications ☆

A.W. Costall *, A. Gonzalez Hernandez [1], P.J. Newton, R.F. Martinez-Botas

Department of Mechanical Engineering, Imperial College London, City and Guilds Building, South Kensington Campus, London SW7 2AZ, UK

HIGHLIGHTS

- We describe a detailed design methodology for ORC radial turbo expanders.
- Toluene is selected as the working fluid for diesel engine waste energy recovery.
- A first turbine of 15.5 kW is designed but yields too small inlet blade heights.
- A second turbine for minimum power generates 34.1 kW with 51.5% efficiency.
- A third turbine for maximum efficiency produces 45.6 kW at 56.1% efficiency.

ARTICLE INFO

Article history:
Received 30 August 2014
Received in revised form 16 February 2015
Accepted 19 February 2015
Available online 13 March 2015

Keywords:
Bottoming cycles
Mobile organic Rankine cycle
Radial turbine
Toluene
Turbo expander
Waste heat recovery

ABSTRACT

Future vehicles for clean transport will require new powertrain technologies to further reduce CO_2 emissions. Mobile organic Rankine cycle systems target the recovery of waste heat in internal combustion engines, with the exhaust system identified as a prime source. This article presents a design methodology and working fluid selection for radial turbo expanders in a heavy-duty off-road diesel engine application. Siloxanes and Toluene are explored as the candidate working fluids, with the latter identified as the preferred option, before describing three radial turbine designs in detail. A small 15.5 kW turbine design leads to impractical blade geometry, but a medium 34.1 kW turbine, designed for minimum power, is predicted to achieve an isentropic efficiency of 51.5% at a rotational speed of 91.7 k min^{-1}. A similar 45.6 kW turbine designed for maximum efficiency yields 56.1% at 71.5 k min^{-1}. This emphasizes the main design trade-off – efficiency decreases and rotational speed increases as the power requirement falls – but shows reasonable radial turbine efficiencies and thus practical turbo expanders for mobile organic Rankine cycle applications are realizable, even considering the compromised flow geometry and high speeds imposed at such small scales.

© 2015 The Authors. Published by Elsevier Ltd. This is an open access article under the CC BY license (http://creativecommons.org/licenses/by/4.0/).

1. Introduction

The global drive towards reducing CO_2 emissions from all forms of transport will require vehicle manufacturers to develop new technology to improve powertrain system efficiency. Despite the growth of the hybrid and electric passenger vehicle segments, internal combustion (IC) engines still power the vast majority of vehicle fleets. In the case of heavy-duty on-highway trucks, and off-road machines in particular, being neither candidates for full electrification nor especially well-suited to hybridization, the ability to reduce CO_2 emissions will depend on improvements in conventional powertrains because the IC engine will continue to be the prime mover for decades to come [1].

1.1. The organic Rankine cycle for waste heat recovery

Considering that ~22–35% [2] of the energy contained in the fuel is rejected to the exhaust, it is clear that waste heat recovery (WHR) technologies represent one of the best routes to achieving the required IC engine system efficiency improvements [3]. Although a significant part of the exhaust enthalpy will be extracted by turbocharging, there still exists an opportunity to recover some of the remaining lower grade heat energy. It is in this category, so-called *bottoming cycles*, where the organic Rankine cycle (ORC) is being investigated.

☆ This paper is included in the Special Issue of Clean Transport edited by Prof. Anthony Roskilly, Dr. Roberto Palacin and Prof. Yan.

* Corresponding author.
E-mail address: a.costall@imperial.ac.uk (A.W. Costall).
[1] Present address: University of Cambridge, Department of Engineering, Trumpington Street, Cambridge CB2 1PZ, UK.

http://dx.doi.org/10.1016/j.apenergy.2015.02.072
0306-2619/© 2015 The Authors. Published by Elsevier Ltd.
This is an open access article under the CC BY license (http://creativecommons.org/licenses/by/4.0/).

Nomenclature

Symbols

A	area (m^2))
B	blockage coefficient (–)
b	blade height (mm)
C	absolute velocity ($m\ s^{-1}$)
D	diameter (mm)
h	enthalpy ($J\ kg^{-1}$)
i	incidence angle (radians)
M	Mach number (–)
$\dot{m}$	mass flow rate ($kg\ s^{-1}$)
N	rotational speed
N_s	specific speed (–)
r	radius (mm)
Re	Reynolds number (–)
s	blade span (mm)
SP	size parameter (m)
t	blade thickness (mm)
U	blade speed ($m\ s^{-1}$)
$\dot{V}$	volume flow rate ($m^3\ s^{-1}$)
V_R	volume flow rate ratio (–)
W	relative velocity ($m\ s^{-1}$)
$\dot{W}$	power (kW)
Z_b	blade number (–)

Greek letters

α	absolute flow angle (radians)
β	relative flow angle (radians)
ϵ	clearance (mm)
η	efficiency (–)
Λ	degree of reaction (–)
Φ	flow coefficient (–)
ϕ	velocity coefficient
Ψ	blade loading coefficient (–)
ρ	density ($kg\ m^{-3}$)
ζ	loss coefficient (–)

Subscripts

0	stagnation value
1	stage inlet station
2	stator outlet or rotor inlet station
3	stage outlet station
act	actual value
av	average
ex	exit
f	effective
geom	geometrical
h	hub
in	inlet station
is	isentropic value
min	minimum value
m	meridional component
N	nozzle
opt	optimum
out	outlet station
R	rotor
r	radial
s	shroud
s	static value
t	total value
win	windage
w	relative component

Superscripts

n	exponent in Table 11

Abbreviations

1D	one-dimensional
3D	three-dimensional
CFD	computational fluid dynamics
D4	octamethylcyclotetrasiloxane
DOE	Department of Energy
IC	internal combustion
MD2M	decamethyltetrasiloxane
MD3M	dodecamethylpentasiloxane
MDM	octamethyltrisiloxane
MM	hexamethyldisiloxane
ORC	organic Rankine cycle
WHR	waste heat recovery

ORC has been applied to WHR in IC engines before [4–7], and even as a direct replacement for a bus engine [8], but has yet to be commercialized, with the additional cost, complexity, and packaging of a mobile ORC system so far proving prohibitive [9]. However, with the aforementioned drive towards lowering CO_2 emissions from heavy-duty vehicles, the recent US DOE-backed *SuperTruck* program developed a mobile ORC system for an American on-highway truck, demonstrating better than 50% brake thermal efficiency [10]. Even so, no such system is known to have been successfully applied to an heavy-duty *off-road* machine.

1.2. Expanders for mobile ORC systems

Selection of the appropriate expander can be made by considering the availability and temperature of the heat source, and the turbine power that can be generated. For the present application these parameters can be determined from knowledge of the range of exhaust gas mass flow rates and temperatures experienced. A comparison of radial, screw, and scroll expanders [11] suggests that for a high temperature WHR application with an expected regenerated power in the order of 15 kW, a radial machine can be considered. Other expander types have also been assessed over the years [12–15].

2. Working fluid selection

2.1. Working fluid selection procedure

Selection of a suitable working fluid is crucial for ORC systems [11,16–18], and influences overall system performance and expander efficiency. The procedure used herein is shown in Fig. 1. Key factors in the selection process include: matching the working fluid critical temperature and that of the heat source (thereby avoiding prohibitive volume ratios across the expander [14,11]); matching the working fluid evaporating temperature and that of the heat source (to reduce irreversibilities [19]); and ensuring good chemical and thermal stability at temperatures well above operating conditions [20].

The preliminary screening step considers whether operation is at close to critical conditions. In the current work, the candidate fluids are down-selected to Toluene and Siloxanes, which have critical temperatures suitable for a ~300 °C heat source.

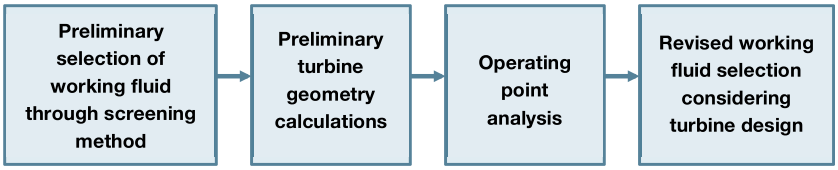

Fig. 1. Working fluid selection procedure.

Table 1
Fluid properties for linear and cyclic Siloxanes and Toluene [16,20,22,23].

Property	Linear siloxanes	Cyclic siloxanes	Toluene
Critical pressure (bar)	8–20	9–13	41
Critical temperature (°C)	245–380	313–372	317
Condensing pressure at 40 °C	>2 kPa	<1 kPa	>3 kPa
Volumetric expansion ratio	Large	Large	Moderate
Outlet volume flow rate	Relatively large	Relatively large	Relatively small
Saturation vapor curve	Dry	Dry	Dry
Molecular weight (kg/kmol)	162–311	296–445	92
Sound speed	Very low	Very low	Low
Specific speed for 20–60 k min^{-1}	MDM, MM in radial turbine range (0.14–0.98) and MD2M, MD3M, MD4M in axial turbine range	Axial turbine range (>1.12, except for D4)	Radial turbine range (0.09–0.28)
Regeneration requirement for high efficiencies	High	High	Moderate
Toxicity	Low	Low	Low–medium
Flammability	Limited	Limited	Flammable
Thermal stability at 400 °C (in absence of oxygen and humidity)	Good	Good	Good

Preliminary turbine geometry calculations are performed, followed by a turbine operating point analysis that examines the effect of changing inlet conditions. The proximity of the working fluid critical conditions is considered in the final step, permitting an opportunity to adjust the operating condition with turbine performance in mind.

2.2. Working fluid requirements and selection criteria

Assumptions:

- Heat energy from the exhaust gases is sufficient to meet ORC operating conditions.
- Only pure working fluids are considered. Azeotropic and zeotropic fluids have been neglected, while acknowledging they could enable power and/or efficiency improvements [14].
- No techno-economic optimization of working fluid selection is performed; the reader is referred to [21].

Fluid properties and reported advantages and disadvantages of linear Siloxanes (MM, MDM, etc.) and Toluene are presented in Table 1, and critical temperatures, pressures, and molecular weights in Table 2. For comparison, critical temperature is plotted against critical pressure in Fig. 2. The critical temperature of MM (245 °C) was considered too low for the heat source temperature. Meanwhile, greater molecular weight implies a higher volumetric expansion ratio (and consequent inlet/outlet area change) across the turbine. For a small-scale, single-stage radial turbine, this should be minimized. Siloxanes with higher molecular weights (MD2M, MD3M, D4, etc.) were thus deemed unsuitable.

Fig. 3 compares the evaporating and condensing temperatures of the two remaining candidates; two different pressure ratios have been plotted to examine the effect on the operating point. In general, greater pressure ratio leads to higher cycle efficiencies and lower regeneration requirements, and so it is desirable to make this as large as possible. However, a single-stage radial turbine will be limited to a pressure ratio of ~25, which will limit the obtainable cycle efficiency. Fig. 3 also highlights the operating region desired for high cycle efficiency and work output, which

Table 2
Some thermodynamic properties of selected linear Siloxanes and Toluene [16].

Long name	Short name	Critical temp. (°C)	Critical pressure (bar)	Molecular weight (kg/kmol)
Hexamethyldisiloxane	MM	245.5	19.1	162.4
Octamethyltrisiloxane	MDM	291.2	14.4	236.5
Decamethyltetrasiloxane	MD2M	326.2	12.3	310.7
Toluene	–	319.0	41.3	92.1

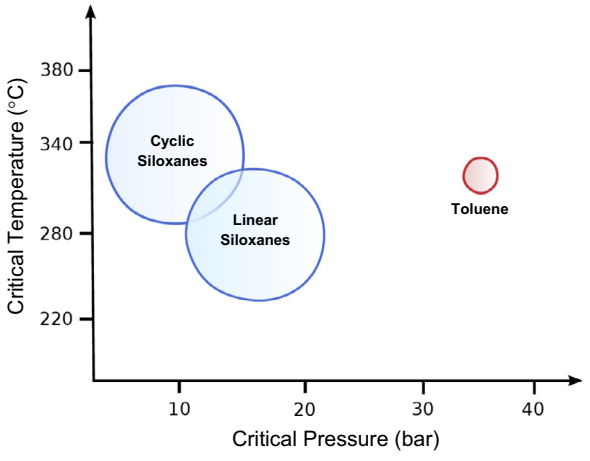

Fig. 2. Critical pressure and temperature range of Siloxanes and Toluene (data from [14]).

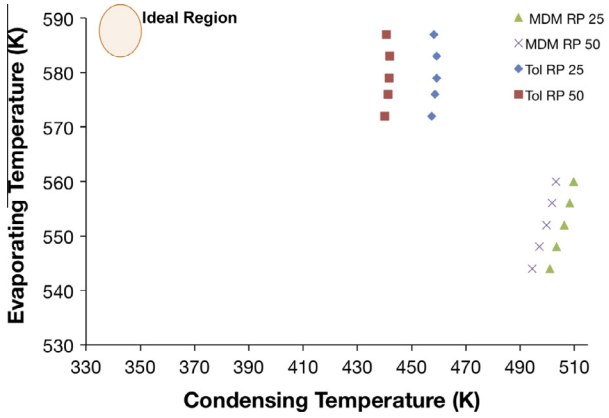

Fig. 3. Evaporating vs. condensing temperature for MDM and Toluene at pressure ratios of 25 and 50 (data from [24]).

ideally requires a much lower condensing temperature than the working fluids under consideration here provide. For the same pressure ratio, Siloxanes experience a much smaller enthalpy drop than Toluene, as observed for MDM in Fig. 3. This drives lower cycle efficiencies for MDM and a corresponding requirement for greater regenerator capacity to recover it [16]. Finally, considering the different working fluid attributes (Fig. 4 and Table 3), Toluene was selected for this small-scale ORC turbine.

3. Design methodology

3.1. General considerations

Important features of the design methodology are:

- The working fluid is treated as a *compressible*, *non-ideal* gas, since the expansion process involves operation at close-to-critical conditions, across large expansion ratios.
- Flow across the expander is assumed steady and adiabatic, although the heat source will be unsteady in a mobile application, and there will inevitably be some degree of heat loss.

Table 3
Comparison between Toluene and MDM (data from [24]).

Criterion	Toluene	MDM
Evaporating temperature (°C)	572.0	552.0
Condensing temperature (°C)	457.4	506.2
Outlet volume flow rate ($m^3\ s^{-1}$)	0.051	0.072
Outlet sound speed ($m\ s^{-1}$)	203.6	132.4
Size parameter, *SP* (m)	0.059	0.10
Volume flow rate ratio, V_R (–)	38.9	45.0
Inlet pressure (MPa)	3.23	1.18
Inlet density ($kg\ m^{-3}$)	125.1	121.4

- The number of stages is limited to one to minimize complexity and cost.
- Radial-fibred blades are not required since material strength is not considered a limiting factor, due to the relatively low enthalpy changes and peripheral speeds.
- Full admission is initially assumed. If blade heights are unsatisfactory under full admission, partial admission will be considered.

3.2. Performance parameters

Total-to-static isentropic efficiency is used since it is assumed that rotor outlet kinetic energy will not be recovered. In Eq. (1), h_{01} denotes the stage inlet stagnation enthalpy, and h_{3act} and h_{3is} the actual and isentropic outlet static enthalpies, respectively.

$$\eta_{t\text{-}s} = \frac{h_{01} - h_{3act}}{h_{01} - h_{3is}} \tag{1}$$

The volume flow rate ratio V_R (Eq. (2)) has a major impact on turbine efficiency and geometry; the high values experienced in the expansion process of organic fluids necessitate a large change in rotor blade height between the inlet and outlet stations.

$$V_R = \frac{\rho_{in}}{\rho_{out}} \tag{2}$$

The specific speed N_s (Eq. (3)) is often employed as a standard index to correlate the flow capacity to the work output of any particular turbomachine [25], and can be used to provide an expectation of attainable efficiency.

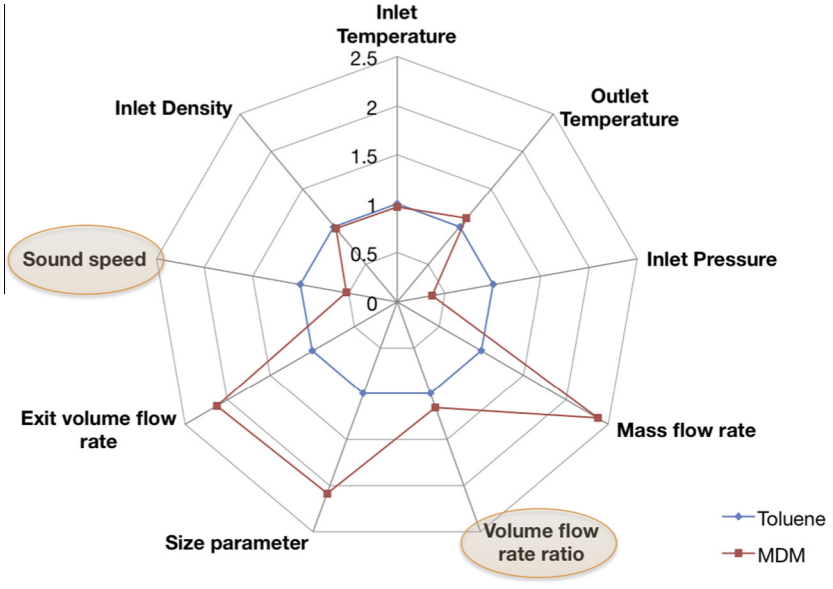

Fig. 4. Comparison between Toluene (as reference) and MDM (data from [24]).

$$N_s = \frac{N \cdot \sqrt{\dot{V}_{ex}}}{h_{is}^{0.75}} \quad (3)$$

The size parameter SP (Eq. (4)) was introduced [17] to indicate the relative size of competing designs, and can be used in a similar fashion to the specific diameter [25,26].

$$SP = \frac{\sqrt{\dot{m}_{out}/\rho_{out}}}{\sqrt[4]{\Delta h_{is}}} \quad (4)$$

3.3. Design parameters

As the inlet blade speed U_2 is limited by mechanical stress considerations (independent of turbine size), high *rotational* speeds are to be expected in turbines with diameters in the order of a few centimeters. It is used here as a main design variable – changing U_2 essentially increases or decreases the inlet relative flow angle β_2 – and a wide range is usually considered in order to explore the effect on rotor performance.

The degree of reaction Λ (Eq. (5)) is the ratio of static enthalpy change occurring across the rotor to the total enthalpy change across the stage as a whole. The lower the reaction, the larger the acceleration across the stator.

$$\Lambda = \frac{(h_2 - h_{3act})}{(h_{02} - h_{03})} = \frac{\left(h_1 - \frac{1}{2}C_{2is}^2 - h_{3act}\right)}{(h_{02} - h_{03})} \quad (5)$$

The flow coefficient Φ (Eq. (6)) is the rotor outlet meridional velocity nondimensionalized by the inlet blade speed [25,26].

$$\Phi = \frac{C_{m3}}{U_2} \quad (6)$$

The blade loading coefficient Ψ (Eq. (7)) represents the work capacity of a turbine stage, defined as the ratio of the total specific enthalpy change to the square of the blade speed [25,26].

$$\Psi = \frac{\Delta h_0}{U_2^2} \quad (7)$$

3.4. Targets, assumptions, and constraints

Various targets, assumptions, and constraints on the rotor design are collated in Table 4. Allowing for the energy extracted by the turbocharger, the temperature of the exhaust gas at the heat exchanger inlet will be ~300 °C giving an energy transfer rate to the ORC system in the range 125–145 kW, based on example engine data [2]. Applying typical cycle efficiencies of 12–18% (as reported by [13,16]) suggests a turbo expander power requirement of 15–26 kW, an approximation that suffices for the purpose of this study. The assumptions and constraints applied to rotor geometry (including the velocity triangles) and operation are given in Table 5.

Table 4
Design targets, assumptions, and constraints.

Parameter	Target, assumption, or constraint
Target application	Waste heat recovery from a ~360 kW heavy-duty diesel engine
Heat source input temperature	Assumed steady 640–840 K
Cycle efficiency	12–18% (assumed, as reported [16,13])
Objective function	Total-to-static isentropic efficiency (no kinetic energy recovered)
Turbine isentropic efficiency	0.75 (used for initial estimate)
Cycle evaporating conditions	Fluid to be kept in saturated conditions – cycle is subcritical
Cycle condensing conditions	Temperature chosen so that fluid condenses at slightly positive atmospheric pressure
Maximum cycle pressure	32.5 bar [27, based on]
Minimum cycle pressure	5 kPa [16, based on]
Pressure ratio	25 (for a single stage configuration)
Maximum stator outlet relative Mach no.	0.96
Maximum rotational speed	80,000 min^{-1} (based on electrical machine considerations)
Compressibility factor, Z	For $Z < 0.93$ fluid cannot be considered ideal; for $Z < 0.8$ fluid is strongly non-ideal [28]

Table 5
Rotor design constraints (Toluene as working fluid).

Parameter	Value
Blade loading coefficient, Ψ (–)	0.9–1.35
Flow coefficient, Φ (–)	0.2–0.4
Degree of reaction, Λ (–)	0.25–0.45
Blade speed to spouting speed ratio (–), U_2/C_0	0.6–0.8
Outlet hub to shroud radius ratio, r_{3h}/r_{3s}	> 0.30[1]
Average outlet radius to inlet radius ratio [25], r_{3av}/r_2	0.6–0.7[2]
Outlet shroud radius to inlet radius ratio, r_{3s}/r_2	< 0.95
Outlet to inlet relative velocity ratio, w_{3av}/w_2	> 1.00
Minimum rotor inlet diameter, r_2 (mm)	20
Nozzle velocity coefficient, Φ_N (–)	0.95
Relative inlet flow angle, β_2 (°)	$-20 < \beta_2 < 0$
Rotor outlet flow angle, α_3 (°)	0
Maximum inlet relative Mach number, M_{w2} (–)	0.96
Maximum outlet relative Mach number, M_{w3} (–)	1.30
Power output, $\dot{W}$ (kW)	15–35
Rotational speed, N (min^{-1})	40,000–190,000

[1] Recommended in [29].
[2] Recommended in [25].

3.5. Velocity triangle design

Fig. 5 shows the standard rotor meanline cross-section of a 90° radial inflow turbine. The stage numbering specified here is used throughout this article.

3.5.1. Basic design concepts

Simplifying the Euler Turbomachinery equation (Eq. (8) [25,26]) by assuming zero rotor outlet swirl gives Eq. (9). Additionally assuming zero pre-swirl, for a given power requirement the minimum allowable U_2 can be calculated from Eq. (10).

$$\frac{\dot{W}}{\dot{m}} = U_2 C_{\theta 2} - U_3 C_{\theta 3} \quad (8)$$

$$\frac{\dot{W}}{\dot{m}} = U_2 C_{\theta 2} \quad (9)$$

$$\frac{\dot{W}}{\dot{m}} = U_2^2 \quad (10)$$

3.5.2. Rotor inlet conditions

The rotor inlet velocity triangles are constrained by the limit imposed on the inlet relative Mach number M_{w2}, which in turn constrains the inlet relative velocity W_2. Applying the minimum blade speed $U_{2\,min}$, calculated using Eq. (10), as an initial condition, the inlet velocity triangle is fully defined (Fig. 6).

As the inlet blade speed is increased from $U_{2\,min}$, the degree of reaction increases (for fixed Φ) as a result of decreasing absolute inlet velocity C_{2is} and thus increasing rotor inlet static enthalpy h_2. The absolute inlet velocity considered in this calculation is the isentropic velocity C_{2is}, which is related to the actual velocity

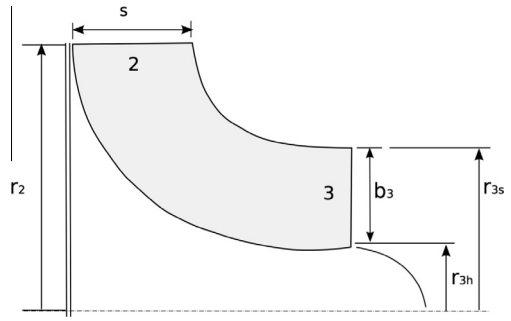

Fig. 5. Definition of rotor station numbering and dimensions in the meridional plane.

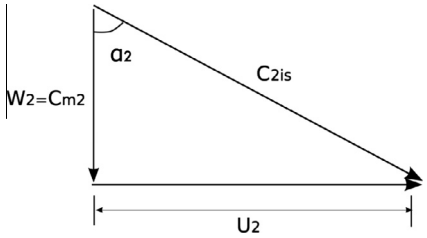

Fig. 6. Inlet velocity triangle nomenclature.

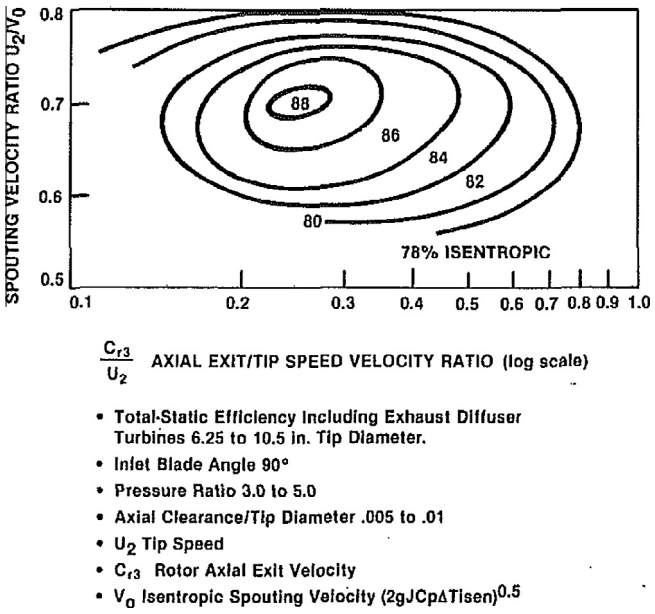

Fig. 7. Attainable efficiency levels of radial inflow turbines [30]. Reprinted with permission of ASME.

C_2 through Eq. (11), which defines the nozzle velocity coefficient, Φ_N. C_2 is then used to find the actual enthalpies h_{2act} and h_{3act}.

$$\Phi_N = \frac{C_2}{C_{2is}} \tag{11}$$

To analyze the effect of Λ on the inlet velocity triangle and blade geometry, a range of blade speeds (see Table 5) were considered. Eq. (5) shows Λ is dependent on the outlet static enthalpy h_{3act}, i.e., the outlet conditions will have an impact, and will need to be determined to fully assess the effect of design parameters on the rotor geometry.

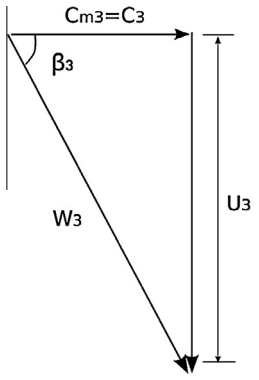

Fig. 8. Outlet velocity triangle nomenclature (zero swirl).

3.5.3. Rotor outlet conditions

The flow coefficient Φ and the ratio of blade speed to spouting speed U_2/C_0 (the "velocity ratio") need to be determined. These parameters are correlated in Fig. 7 to provide an estimate of the efficiency, at least for conventional radial turbines [30]. The figure indicates a velocity ratio range of $0.6 < U_2/C_0 < 0.75$, and a flow coefficient range of $0.2 < \Phi < 0.4$ should generate the highest efficiencies. Although this will not be valid for ORC turbines, a similar trend is assumed to establish a starting point in the present work.

In contrast to the inlet rotor conditions, for which velocity triangles have yet to be fixed, it is assumed that the rotor outlet will contain zero swirl. This imposes the velocity relationship shown in Fig. 8; after selecting a flow coefficient Φ, and having knowledge of the outlet stagnation enthalpy, the static enthalpy (for each flow coefficient) can be determined from Eq. (12).

$$h_{3is} = h_{03} - \frac{1}{2}C_3^2 \tag{12}$$

From the outlet velocity triangle, Eq. (14) can be derived [25]. This expression is used to obtain the outlet flow angle β_{3av} at the mean radius. As previously mentioned, the ratio r_{3av}/r_2 is used as an input variable, so by considering a range of flow coefficients, different outlet velocity triangles may be obtained.

$$h_{3act} = h_{01} - \eta_{t\text{-}s}(h_{01} - h_{3is}) \tag{13}$$

$$\left(\frac{C_{m3}}{U_2}\right) = \left(\frac{r_{3av}}{r_2}\right) \cdot \cot\beta_{3av} = \left(\frac{r_3}{r_2}\right) \cdot \cot\beta_3 \tag{14}$$

Fig. 9 shows a flow chart of the velocity triangle design procedure, including the method to determine the outlet velocity triangle.

3.5.4. Determining the density at stator outlet

The calculated degree of reaction is then used as an input in an Excel program, which imports relevant fluid properties from REFPROP [24] to calculate the stator outlet enthalpy (i.e., rotor inlet h_2) and density. The outlet meridional velocity C_{m3}, together with the inlet and outlet total enthalpies h_{01} and h_{03} are required as inputs in order to perform calculations using the definition of reaction in Eq. (5).

3.6. Geometry design

3.6.1. Geometrical and effective area

Employing mass conservation, the annular inlet area $A_{geom}2$ can be obtained from Eq. (15) by assuming a mass flow rate $\dot{m}$, knowing the inlet density ρ_2 and the inlet meridional velocity C_{m2}.

$$\dot{m} = \rho_2 \cdot A_{geom2} \cdot C_{m2} \tag{15}$$

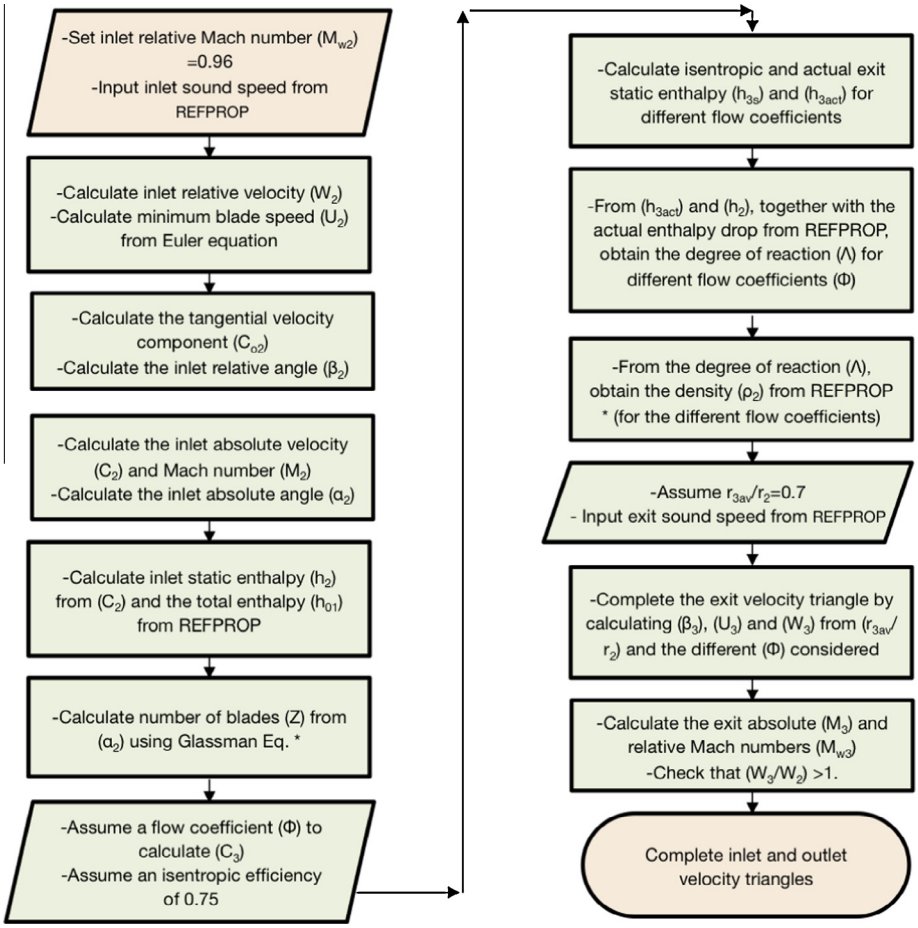

Fig. 9. Design methodology (∗ indicates information from [31]).

Since the full peripheral (at the inlet) or annular (at the outlet) areas are not available due to the presence of the blades, a blockage coefficient B is introduced, e.g., at the rotor inlet the geometrical area A_{geom2} and the effective area A_{f2} are related by Eq. (16).

$$A_{f2} = (1 - B_2) \cdot A_{geom2} \tag{16}$$

The blockage coefficient accounts for the area due to the blade thickness t, computed using Eq. (17), where Z_b is the blade number and s is their span. Fig. 10 illustrates the blockage effect at the rotor exit.

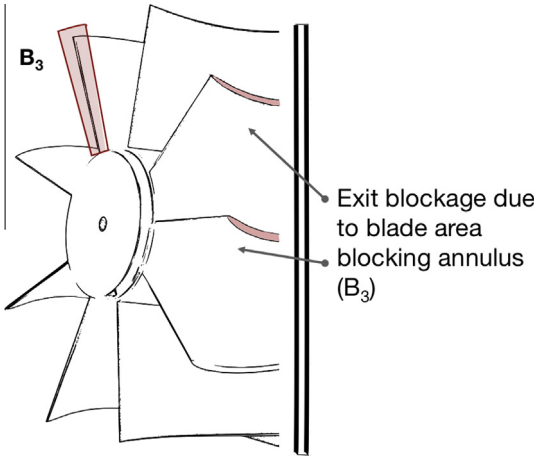

Fig. 10. Illustration of blockage.

$$B_2 = \frac{(Z_b \cdot t \cdot s)}{A_{geom2}} \tag{17}$$

Even though B_2 will change between individual designs, a single value (refer to Table 9) has been assumed for the geometries calculated here. Knowing the inlet effective area A_{f2}, the inlet radius r_2 can be determined by assuming a value for the inlet span s in Eq. (18).

$$r_2 = \frac{A_{f2}}{2 \cdot \pi \cdot s} \tag{18}$$

This defines the inlet geometry. The outlet geometry is then calculated using Eq. (19) and knowledge of the outlet density ρ_3 and an assumed value of C_{m3} (which depends on the selected values of Φ and U_2).

$$\dot{m} = \rho_3 \cdot A_{geom3} \cdot C_{m3} \tag{19}$$

A larger value for the outlet blockage coefficient B_3 was chosen (see Table 9) to calculate the effective outlet area A_{f3}, since the blades occupy a larger portion of the outlet flow area, compared to the inlet. The calculation of B_3 is not as straightforward, since a streamwise analysis would need to be performed before the actual outlet geometry is completely defined. The outlet shroud and hub radii are calculated by assuming a value for the hub to shroud radius ratio, r_{3h}/r_{3s}, as per Eq. (20).

$$r_{3s} = \sqrt{\frac{A_{f3}}{\pi \cdot \left(1 - \left(\frac{r_{3h}}{r_{3s}}\right)^2\right)}} \tag{20}$$

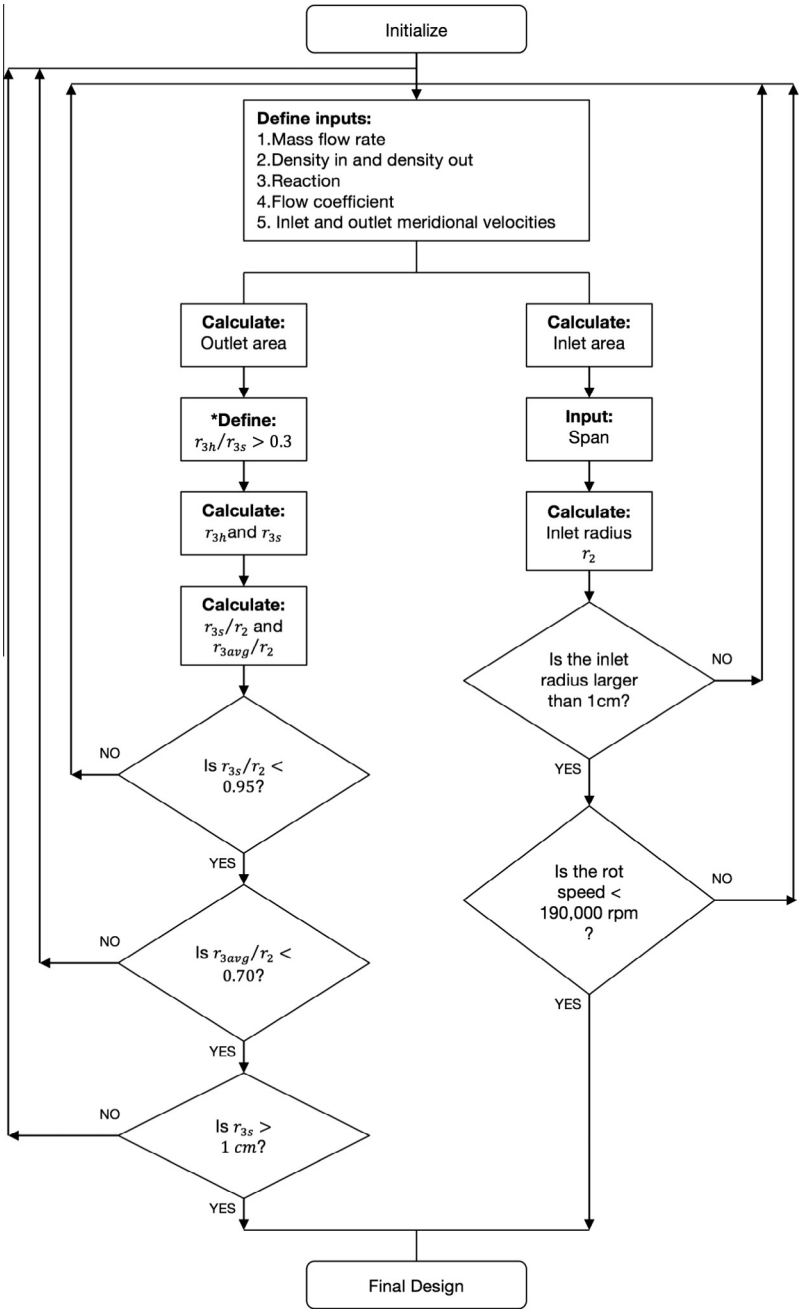

Fig. 11. Geometry definition procedure (∗ indicates assumption).

3.6.2. Blade number

In order to calculate the blade number, the empirical relationship of Glassman (Eq. (21)) is employed [25].

$$Z_b = \frac{\pi}{30} \cdot (110 - \alpha_2) \cdot \tan \alpha_2 \tag{21}$$

The full procedure used to establish the rotor geometry is given in Fig. 11.

3.7. Performance prediction by loss coefficient evaluation

A prediction of turbine performance based on geometrical parameters is required to evaluate competing designs. For conventional radial turbines, a loss analysis can be employed based on the calculation of a number of loss coefficients [31]. Their application to organic fluids is discussed below.

3.7.1. Incidence loss

Incidence loss will be based on the change in the tangential component of kinetic energy [as per 26,31]. The optimum relative flow angle $\beta_{2,opt}$ is defined as that at which there is no change in the tangential velocity component [31], computed using Eq. (22).

$$\tan \beta_{2,opt} = \frac{(-1.98 \cdot U_2)}{(Z_b \cdot C_{m2})} \tag{22}$$

The incidence loss is then expressed as an enthalpy change (later represented as an efficiency deficit), in Eq. (23) [as per 25], where the exponent n depends on whether the incidence is positive or negative ($n = 2.5$ for $i > 0$; $n = 1.75$ for $i < 0$).

$$\Delta h_i = \frac{1}{2} W_2^2 (1 - \cos^n i_2) \tag{23}$$

3.7.2. Nozzle loss coefficient

The nozzle loss coefficient is defined in [25] as:

$$\zeta_N = \frac{(h_2 - h_{2is})}{\frac{1}{2}C_2^2} \tag{24}$$

The velocity coefficient (Eq. (11)) is related to the enthalpy loss coefficient through:

$$\zeta_N = \frac{1}{\phi_N^2} - 1 \tag{25}$$

For well-designed stators in conventional turbines, ϕ_N ranges between 0.90 and 0.97 [25]. An intermediate value of 0.95 is selected as an initial guess in the design procedure. The selection of a nozzle loss coefficient establishes the nozzle efficiency as:

$$\eta_N = \frac{1}{(1 + \zeta_N)} \tag{26}$$

The effect of ζ_N is to reduce the absolute rotor inlet velocity and therefore the meridional inlet velocity, consequently increasing the ratio C_{m3}/C_{m2} across the rotor.

3.7.3. Rotor loss coefficient

In the case of ORC turbine design, the rotor loss coefficient will be defined in such a way to absorb other losses and is expressed in [25] as:

$$\zeta_R = \frac{(h_3 - h_{3is})}{\frac{1}{2}W_3^2} \tag{27}$$

The velocity coefficient is given as:

$$\phi_R = \frac{W_2}{W_{3is}} \tag{28}$$

This is related to the enthalpy loss coefficient through:

$$\zeta_R = \frac{1}{\phi_R^2} - 1 \tag{29}$$

For well-designed rotors in conventional turbines, ϕ_R ranges between 0.70 and 0.85 [25]. In contrast to the treatment of the stator velocity coefficient, there is no need to assume a value for the rotor loss coefficient ζ_R, since a value for the initial isentropic efficiency has already been defined.

Combining rotor, nozzle, and incidence loss coefficients [25], gives:

$$\eta_{t\text{-}s} = 1 - \frac{\left(C_3{}^2 + \zeta_N \cdot C_2^2 + \zeta_R \cdot W_3^2 + (1 - \cos^n i_2) \cdot W_2^2\right)}{C_0^2} \tag{30}$$

3.7.4. Tip clearance loss

For the cases considered here, involving extremely small spans, the radial clearance must be reduced to 0.25 mm to maintain the tip leakage within acceptable levels. Several empirical models for clearance loss have been proposed. An expression in terms of inlet blade height and the ratio of outlet to inlet mean radii, and the radial clearance ϵ_r, is given in [32] as:

$$\Delta\eta_{t\text{-}t} = 2\frac{\epsilon_r}{s} \cdot \left(\frac{r_{3av}}{r_2} - 0.275\right) \tag{31}$$

3.7.5. Windage loss

The loss of specific work due to the windage can be expressed [26] as:

$$\Delta h_{win} = \frac{0.56 \cdot \rho_2 \cdot D_2^2 \cdot (U_2/100)^3}{\dot{m} \cdot Re} \tag{32}$$

3.7.6. Shock loss

The rotor inlet relative Mach number M_{w2} has been limited to 0.96, and thus transonic flow will occur across the rotor stage. As sonic conditions are reached at the stator outlet, shock losses will take place at the rotor entry and through the passage, and are also likely to be present at rotor outlet. The expressions found in the literature [26, e.g.] rely on ideal gas laws and cannot be applied here. Additionally, the conventional method for accounting for shock losses may not be applicable to organic fluids operating near critical conditions. Hence it is worth considering that additional losses will be present and that the true isentropic efficiency is expected to be lower than that predicted in this study.

4. Design results

Three different radial turbine designs are now presented: (i) a *small* turbine designed to meet the low power requirement, (ii) a *medium* turbine, also designed for minimum power but which meets an additional geometry constraint on inlet blade height, and (iii) a *large* turbine meeting the same constraints as (ii) but designed for maximum isentropic efficiency. Note that the labels small, medium, and large are only used here to clearly distinguish the three designs, rather than as an indication of size.

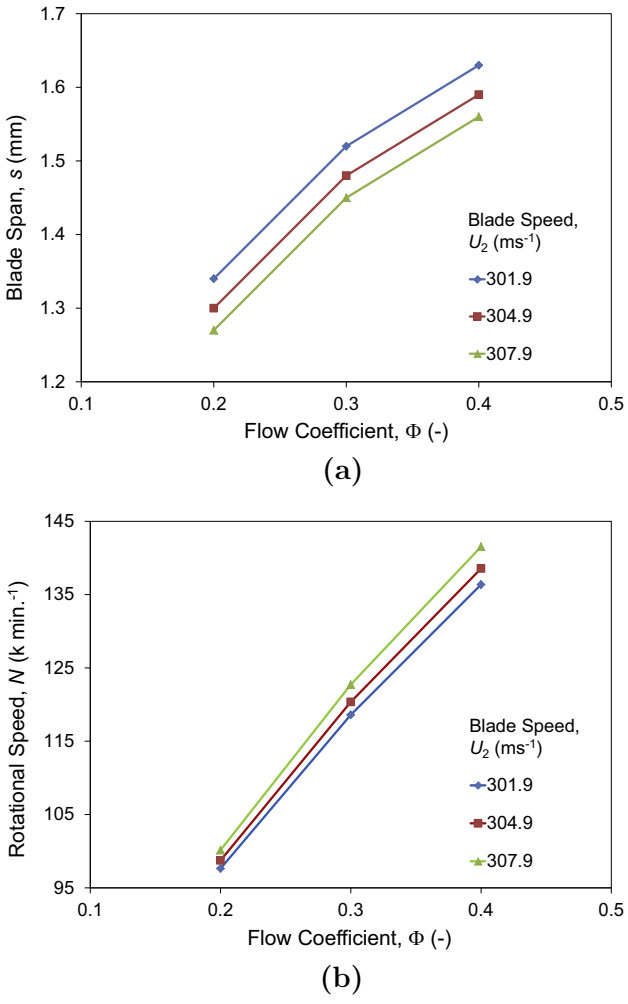

Fig. 12. Effect of flow coefficient and blade speed on (a) blade span, and (b) rotational speed – small turbine.

4.1. Small turbine

This option was designed for the low end of the expected turbine power requirement (15–26 kW). In Fig. 12 both the span and rotational speed increase with the flow coefficient Φ. The higher the inlet blade speed, the smaller the span for the same flow coefficient (and the higher the rotational speed). So a high Φ and a small U_2 are beneficial to promote larger inlet blade heights, especially important at this small scale, but at the cost of higher rotational speed and smaller inlet and outlet radii. Nevertheless, by selecting the minimum possible blade speed of 301.9 m s^{-1} (which corresponds to an axial inlet to the stage, i.e., the minimum blade speed without pre-swirl), the rotational speed can be reduced somewhat, while the span can be increased.

Operating point and geometrical data for the resulting 15.5 kW turbine are listed in the first data column in Table 9. In this case, the design is specified such that the largest possible inlet blade height is generated whilst complying with all other design constraints. Despite this, the resulting inlet blade height of 1.6 mm is still too small to be practical, and so the estimation of isentropic efficiency was not carried out and hence is not included. The inlet and outlet velocity triangles at mean radius for this turbine are shown in Fig. 13, together with an illustration of the rotor geometry in the meridional plane. The resulting shape is mainly due to the imposed design constraints, which limit the outlet-to-inlet tip radius ratio to a maximum of 0.95, giving rise to a blade profile that has significant sections of constant shroud radius. The significant change in density across the passage is the reason for the large variation in blade height.

The hub and shroud outlet velocity triangles shown in Fig. 14 were calculated using the assumptions of constant axial velocity (C_{m3}) and constant rotational speed along the radius. All velocity triangle parameters for this turbine can be found in Table 6, where it can be seen that a higher relative velocity (and Mach number) is reached at the shroud. Increasing the flow coefficient Φ raises the outlet meridional velocity C_{m3} and thus reduces the outlet relative flow angle β_3. Since the outlet blade speed U_3 remains close to constant, the outlet relative velocity W_3 will also increase.

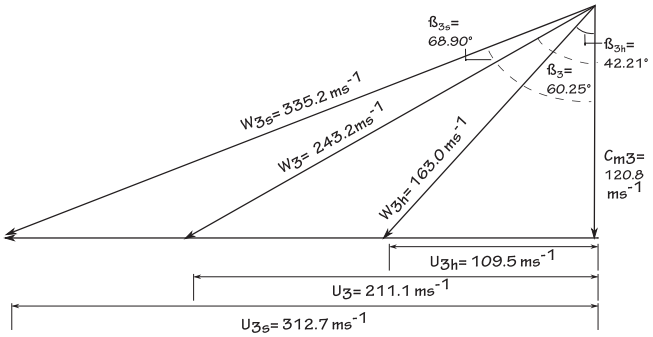

Fig. 14. Outlet velocity triangles at hub and shroud – small turbine.

Table 6
Velocity triangle data – small turbine.

Parameter	*Rotor inlet*	*Rotor outlet*		
		Hub	Mean	Shroud
Radius, r (mm)	21.1	7.0	13.6	20.1
Blade speed, U (m s^{-1})	301.9	109.5	211.1	312.7
Absolute velocity, C (m s^{-1})	354.7	120.8	120.8	120.8
– Meridional component, C_m	186.2	120.8	120.8	120.8
Absolute angle, α (°)	58.3	0	0	0
Absolute Mach no., M (–)	1.83	0.616	0.616	0.616
Relative velocity, W (m s^{-1})	186.2	163.0	243.2	335.2
Relative angle, β (°)	0	42.2	60.2	68.9
Relative Mach no., M_W (–)	0.96	0.832	1.24	1.71
Density, ρ (kg m^{-3})	4.45	1.34	1.34	1.34

Increasing the blade loading coefficient Ψ leads to a decrease in inlet meridional velocity C_{m2}, an increase in the inlet relative flow angle β_2, and a decrease in the inlet tangential velocity $C_{\theta 2}$ and absolute flow angle α_2. This also leads to an increase in reaction, which increases the density ratio across the rotor passage. The same effects apply for both this small turbine, and the medium and large turbine designs that follow.

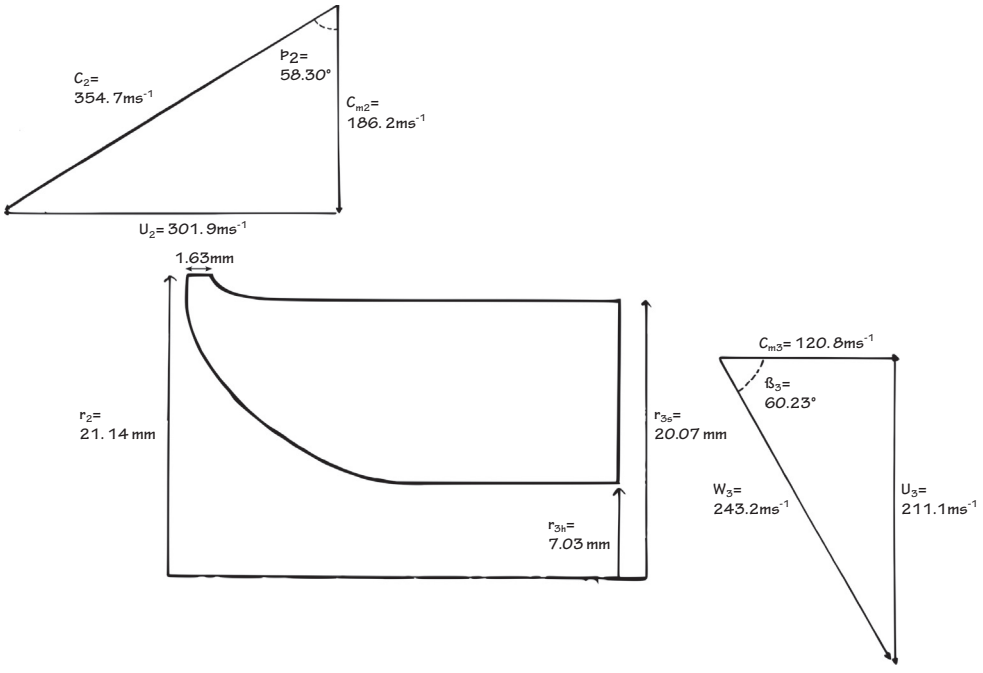

Fig. 13. Rotor geometry, inlet and outlet velocity triangles at mean radius – small turbine.

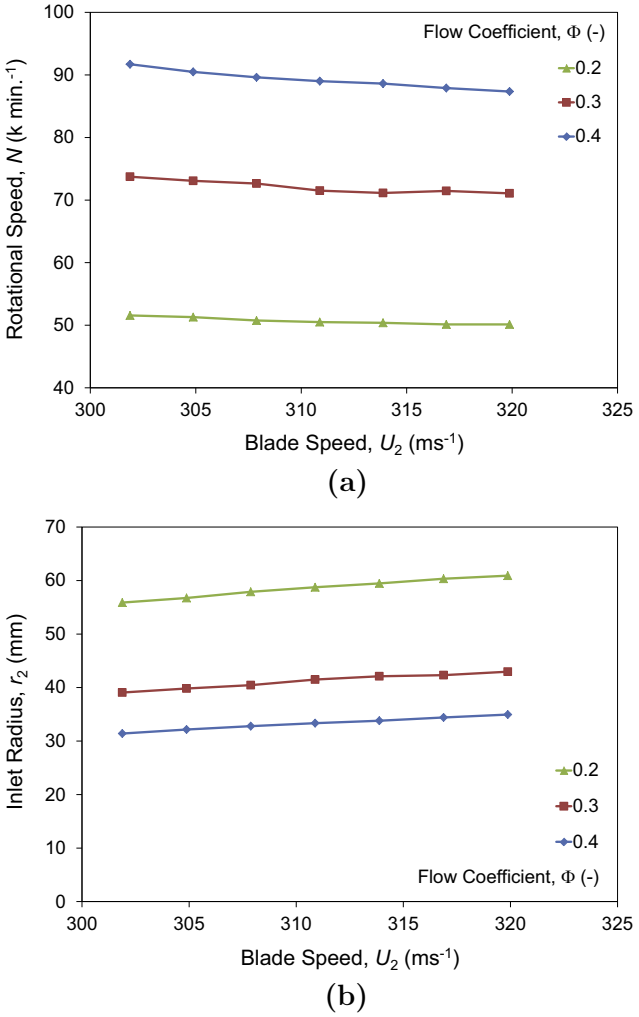

Fig. 15. (a) Effect of flow coefficient on rotational speed, and (b) inlet radius variation with blade speed – medium turbine.

Table 7
Velocity triangle data – medium turbine.

Parameter	*Rotor inlet*	*Rotor outlet*		
		Hub	Mean	Shroud
Radius, r (mm)	21.1	10.5	20.3	30.0
Blade speed, U (m s^{-1})	301.9	109.5	211.1	312.7
Absolute velocity, C (m s^{-1})	354.7	120.8	120.8	120.8
– Meridional component, C_m	186.2	120.8	120.8	120.8
Absolute angle, α (°)	58.3	0	0	0
Absolute Mach no., M (–)	1.74	0.616	0.616	0.616
Relative velocity, W (m s^{-1})	186.2	163.0	243.2	335.2
Relative angle, β (°)	0	42.2	60.2	68.9
Relative Mach no., M_W (–)	0.96	0.832	1.24	1.71
Density, ρ (kg m^{-3})	6.585	1.339	1.339	1.339

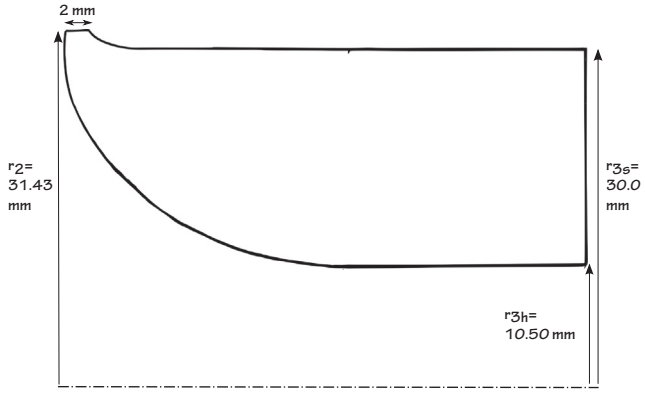

Fig. 16. Rotor geometry – medium turbine.

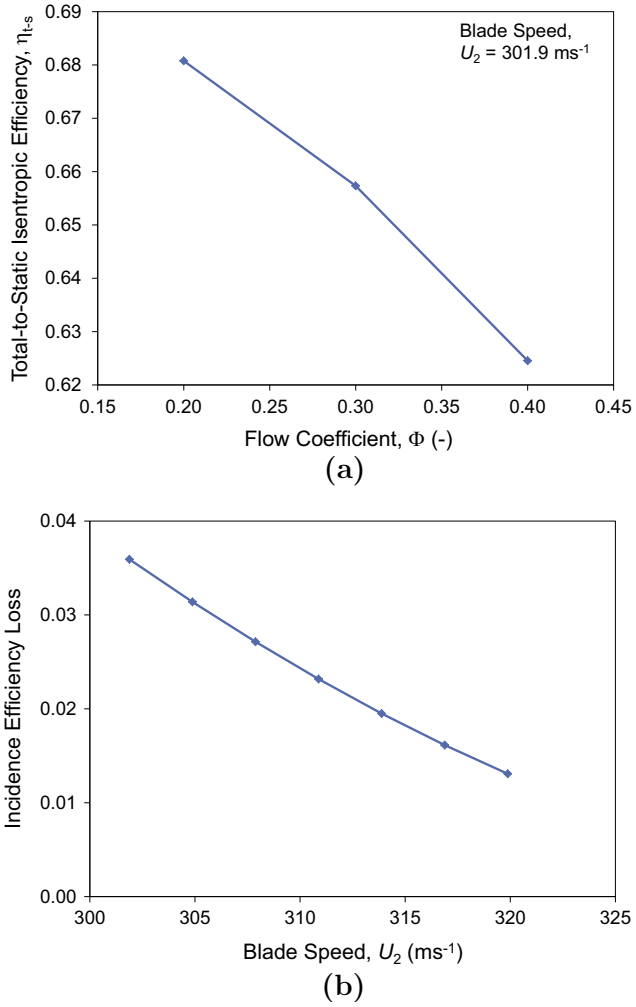

Fig. 17. Effect of (a) flow coefficient on efficiency, and (b) blade speed on incidence efficiency loss.

4.2. Medium turbine

This turbine has been designed with the objective of minimizing power output, while requiring a reasonable rotor geometry. Fig. 15(a) shows that the rotational speed of the turbine is strongly affected by the choice of flow coefficient (Φ), yet is quite insensitive to the blade speed (U_2), within the range shown. This is because a higher Φ will generate greater outlet static enthalpy and higher reaction. This in turn leads to higher inlet density and thus a smaller inlet radius, as indicated by Fig. 15(b). So, the higher the Φ, the smaller the mass flow rate required to comply with the design constraints, and thus to target minimum power output, a higher Φ is beneficial for generating reasonable rotor geometries.

To recap, the inlet blade height of the small turbine was too small. Hence the medium turbine has been designed to generate

the lowest power output while maintaining a minimum inlet blade height of 2 mm, representing the minimum feasible value for wheel manufacture. The rest of the specification has been carried forward, i.e., the inlet and outlet velocity triangles are identical to those for the small turbine (refer to Fig. 13). Even though the small and medium turbines have the same inlet and outlet velocity triangles *at mean radius*, those at the outlet of the hub and shroud will differ due to the change in rotor geometry, as listed in Table 7.

The resulting performance and geometrical data for this 34.1 kW turbine are shown in the second data column in Table 9. This design has a lower rotational speed but the density ratio is much higher compared to the small turbine, but there is only a slight change in tip radius between inlet and outlet of the rotor passage. This is due to the outlet to inlet tip radius ratio constraint, stated in Table 9, which is intended to reduce blade curvature. Although this generates small blade heights, not constraining this ratio will lead to unreasonable geometries.

Fig. 16 shows the rotor blade profile for the medium turbine is not too dissimilar from that for the small turbine. While the radii and axial length of the medium turbine have grown to accommodate the increase in power output, the geometrical constraints are the same as before, except for the imposed 2 mm minimum inlet blade height.

4.3. Large turbine

Fig. 17(a) shows that the higher the flow coefficient Φ, the lower the isentropic efficiency (for a given blade speed). This is primarily due to rising rotor (and nozzle) losses with increasing outlet velocities (and thus with increasing Φ). If the blade speed is increased, there will be a detrimental effect on the flow coefficient and, to a much lesser extent, the passage loss coefficient. Increasing the blade speed for a given Φ leads to higher isentropic efficiencies however, due to the lower level of incidence loss, as illustrated in Fig. 17(b).

Hence to generate a high efficiency design, a lower flow coefficient was selected, and the blade speed (U_2) was permitted to increase since less incidence loss will be experienced at higher speeds, again giving rise to higher isentropic efficiency (which can be considered insensitive to Φ). The final constraint applied to this design was an upper power limit of ~45 kW. The resulting design and operating performance parameters for a turbine designed for maximum efficiency while meeting the stated constraints are given in the third data column in Table 9. The rotational speed has now dropped to ~71.5 k min^{-1}, and the predicted isentropic efficiency has increased by almost five points, to 56%. The inlet and outlet velocity triangles at mean radius for

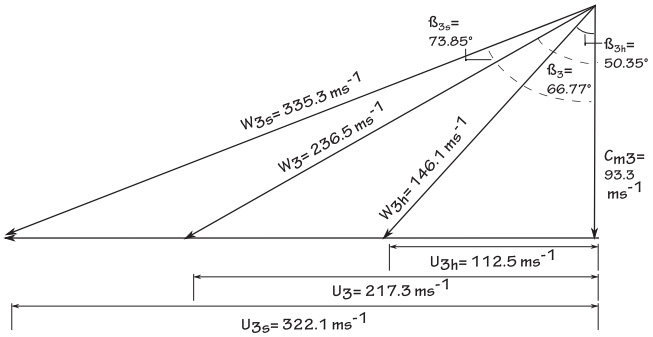

Fig. 19. Outlet velocity diagrams at hub and shroud – large turbine.

Table 8
Velocity triangle data – large turbine.

Parameter	*Rotor inlet*	*Rotor outlet*		
		Hub	Mean	Shroud
Radius, r (mm)	41.5	13.8	26.7	39.5
Blade speed, U (m s^{-1})	310.9	112.5	217.3	322.1
Absolute velocity, C (m s^{-1})	346.9	93.3	93.3	93.3
– Meridional component, C_m	185.4	93.3	93.3	93.3
Absolute angle, α (°)	57.7	0	0	0
Absolute Mach no., M (–)	1.70	0.476	0.476	0.476
Relative velocity, W (m s^{-1})	186.2	146.1	236.5	335.3
Relative angle, β (°)	5.46	50.4	66.8	73.9
Relative Mach no., M_W (–)	0.96	0.75	1.24	1.71
Density, ρ (kg m^{-3})	6.64	1.34	1.34	1.34

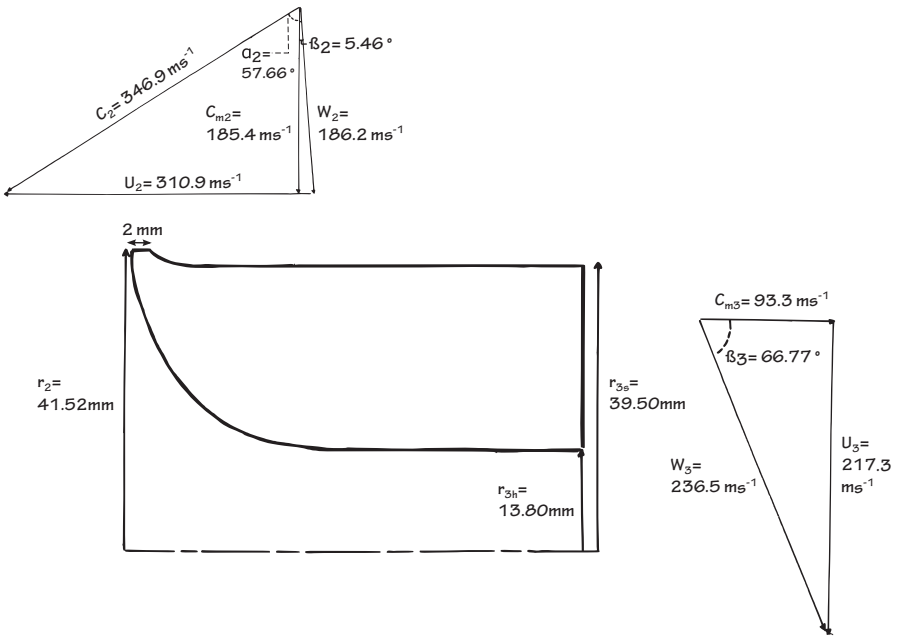

Fig. 18. Rotor geometry, inlet and outlet velocity triangles at mean radius – large turbine.

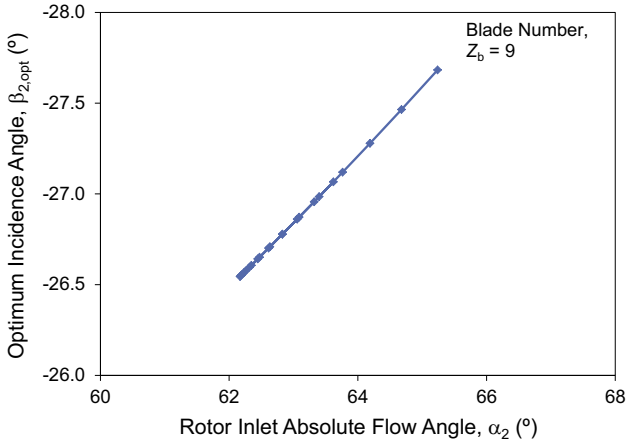

Fig. 20. Optimum rotor incidence angle vs. absolute flow angle – large turbine.

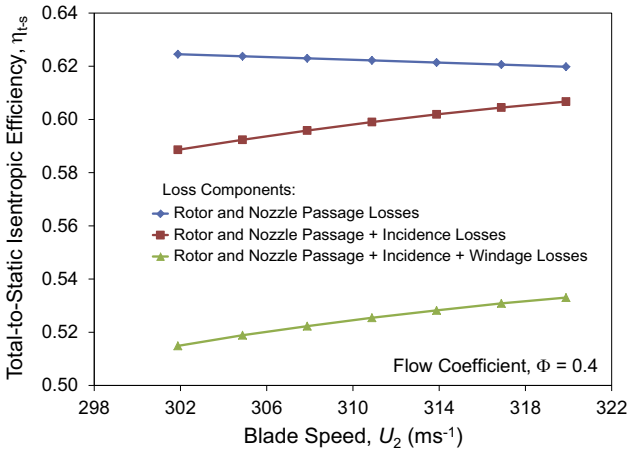

Fig. 21. Contribution of component losses to efficiency for $\Phi = 0.4$.

Table 9
Turbine operating point and design parameters.

Parameter	Small	Medium	Large
Operation			
Rotational speed, N (min^{-1})	136,373	91,705	71,502
Isentropic power, $\dot{W}$ (kW)	15.5	34.1	45.6
Mass flow rate, $\dot{m}$ (kg s^{-1})	0.168	0.370	0.495
Total-to-static isentropic efficiency, η_{t-s} (%)	N/A[1]	51.5	56.1
Reaction, Λ (–)	0.370	0.437	0.440
Blade loading coefficient, Ψ (–)	1.33	1.33	1.26
Flow coefficient, Φ (–)	0.40	0.40	0.30
Specific speed, N_s (–)	0.770	0.518	0.404
Blade number, Z_b (–)	8	9	9
Compressibility factor, Z_{in} (–)	0.767	0.767	0.767
Geometry			
Inlet tip radius, r_2 (mm)	21.1	31.4	41.5
Outlet tip radius, r_3 (mm)	20.1	30.0	39.5
Inlet blade height, b_2 (mm)	1.6	2.0	2.0
Outlet blade height, b_3 (mm)	13.1	19.5	26.0
Inlet blockage, B_2 (–)	0.064	0.050	0.050
Outlet blockage, B_3 (–)	0.080	0.080	0.080
Outlet shroud to inlet radius ratio (constraint), r_{3s}/r_2	0.95	0.95	0.95
Outlet mean to inlet radius ratio (constraint), r_{3av}/r_2	0.64	0.64	0.64

[1] Design of the small turbine was halted prior to efficiency calculation.

Table 10
Comparison of radial turbo expanders in the range 20–50 kW.

Parameter	Large	Comparison 1 [27]	Comparison 2 [15]
Operation			
Working fluid	Toluene	N-pentane	R245fa
Power output (kW)	45.6	50.0	24.0
Evaporating temperature (K)	502.7	420	N/A
Evaporating pressure (bar)	12.3	10.0	34.0
Pressure ratio over turbine	25.0	11.1	13.6
Condensing temperature (K)	411.7	365–370	425
Condensing pressure (bar)	0.491	0.90	2.50
Mass flow rate (kg/s)	0.495	0.670	0.750
Specific enthalpy drop (kJ/kg)	121.5	108.0	N/A
Specific speed	0.404	0.098	0.85
Rotational speed (min^{-1})	71,502	52,085	70,000
Total-to-static isentropic efficiency, η_{t-s} (%)	56.1	69.0	79.0
Geometry			
Degree of reaction	0.440	0.260	0.600
Stage loading	1.26	1.70	N/A
Inlet blade height (mm)	2.0	13.1	1.6
Outlet blade height (mm)	13.8	16.7	25.4
Inlet diameter (mm)	83.0	76.9	59.3
Outlet diameter (mm)	78.9	80.3	42.4

this design are illustrated alongside the blade geometry in Fig. 18. Outlet velocity triangles for the hub and shroud are shown in Fig. 19. All velocity triangle parameters for this design are listed in Table 8.

4.4. Large turbine performance analysis

The optimum incidence angle, $\beta_{2,opt}$, can be calculated using Eq. (22). The relationship between the optimum incidence angle and the inlet absolute flow angle is plotted in Fig. 20. The values obtained for both α_2 and $\beta_{2,opt}$ are within the same range as those seen in conventional radial inflow turbines [31]. The trend followed is also similar, although a smaller variation in $\beta_{2,opt}$ is observed.

Fig. 21 shows the decrease in η_{t-s} caused by the combination of the different loss contributions. It can be observed that the incidence loss decreases with increasing U_2, whilst the windage loss remains relatively constant throughout, and the passage losses increase with increasing U_2, the largest contribution coming from the latter. Note that Fig. 21 is most representative of the medium turbine since the loss data is plotted for a flow coefficient of 0.4. Indeed, Fig. 21 shows that the isentropic efficiency at a inlet blade speed of 302 m s^{-1} (that of the medium turbine, Table 6) is ~52%, which agrees with the value calculated for the medium turbine (51.5% in Table 9).

4.4.1. Comparison with ORC radial turbo expanders in the literature

Table 10 compares the large turbine against similar designs from the literature. Despite similar power outputs, the comparison designs are geometrically quite different, likely due to different working fluids and design constraints. However a large change in blade height from inlet to outlet, and a correspondingly small change in tip radius, is characteristic of all designs.

Comparison Turbine 1 [27] accommodates inlet pre-swirl (β_2 is positive). Pre-swirl has not been considered here to avoid the significant impact on incidence loss, but it does permit smaller values of U_2. Although Comparison Turbine 2 [15] has an efficiency of 79%, the blade inlet height is only 1.6 mm. In a further example, the 0.7–0.8 mm blade heights specified for a mini-ORC system using

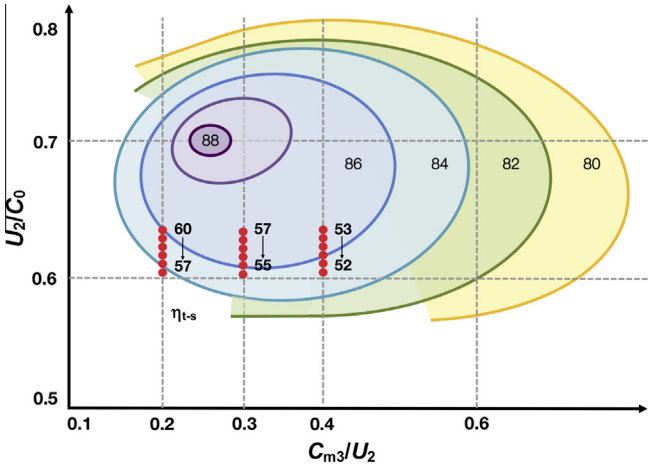

Fig. 22. Predicted large ORC turbine performance (red circles) plotted against conventional radial turbine performance (contours) [30]. Reprinted with permission from ASME. (For interpretation of the references to color in this figure legend, the reader is referred to the web version of this article.)

Table 11
Comparison of the large ORC and conventional (air) radial turbine designs in the range 40–50 kW.

Parameter	Large	Conventional [33]
Operation		
Working fluid	Toluene	Air
Power output (kW)	45.6	49.4
Evaporating temperature (K)	502.7	332.9
Evaporating pressure (bar)	12.3	2.19
Pressure ratio over turbine	25	2.15
Condensing temperature (K)	411.7	271.4
Condensing pressure (bar)	0.491	1.013
Mass flow rate (kg/s)	0.495	0.750
Specific enthalpy drop (kJ/kg)	121.5	61.8
Specific speed	0.404	0.098
Rotational speed (min^{-1})	71,502	52,085
Total-to-static isentropic efficiency, $\eta_{t\text{-}s}$ (%)	56.1	76.5
Geometry		
Inlet blade height (mm)	2.0	18.4
Outlet blade height (mm)	13.8	28.1
Inlet diameter (mm)	83.0	36.0
Outlet diameter (mm)	78.9	80.0

Toluene as the working fluid [16] are also not considered practical, nor is the rotational speed of 182.3 k min^{-1}.

4.4.2. Comparison with conventional radial turbine designs in the literature

Fig. 22 shows the values of $\eta_{t\text{-}s}$ predicted for the ORC turbines as a function of the flow coefficient Φ, which are much lower than can be achieved by conventional turbines [30]. One of the main differences between the radial inflow turbines in this study and that presented in Table 11 is the much lower pressure ratio experienced across the conventional radial turbine. The maximum specific work done across a single stage would limit the pressure ratio across a conventional turbine expanding air or exhaust gas. The change in inlet to outlet tip radius in ORC turbine designs is much smaller than for the conventional turbine, leading to different rotor geometries.

5. Conclusions

This work developed a procedure for the design of practical radial turbo expanders for mobile ORC applications, recognizing the interdependence between expander design and working fluid selection, using the REFPROP database [24] to account for real gas effects. Siloxanes and Toluene were down-selected due to their high critical temperatures, which align with the ~300 °C heat source; Toluene was identified as the more suitable overall.

Three different turbine designs were presented: a small turbine (~20 mm dia.) generating 15.5 kW at ~136 k min^{-1} that meets the low power requirement but requires a ~1.6 mm inlet blade height; a more practical medium turbine (62.9 mm) producing 34.1 kW with 51.5% efficiency at ~91.7 k min^{-1}; and a large turbine (83.0 mm) making 45.6 kW at ~71.5 k min^{-1}, designed for maximum isentropic efficiency (56.1%). These show that reducing the power level compromises isentropic efficiency, with the largest loss contributions originating in the rotor and nozzle passages. A major issue for small-scale ORC radial turbines is the high inlet density and density ratio, leading to extremely small inlet blade heights of a few millimeters, and a large variation between inlet and outlet blade heights.

The novelty of the current work lies in the combination of: (i) the down-selection of Toluene as the working fluid, (ii) the design of radial turbo expanders with explicit provision of the loss equations and procedure employed, and (iii) its application to WHR in a mobile, heavy-duty off-road diesel engine. Future work will integrate the turbine design methodology within a larger ORC design process, comprising a 1D engine model (simulating the transient heat source) and a thermodynamic system model, and will refine the turbine design in 3D CFD. Once these components are in place, it should be feasible to optimize ORC turbo expander design and overall cycle efficiency over a real-life machine duty cycle.

References

[1] Automotive Council UK. Commercial vehicle & off-highway low carbon technology roadmap; 2011.
[2] Heywood JB. Internal combustion engine fundamentals. 1st ed. McGraw-Hill; 1988.
[3] Greszler A. View from the bridge – commercial vehicle perspective. In: Proceedings of the 18th directions in engine-efficiency and emissions research (DEER) conference; 2012. <http://energy.gov/sites/prod/files/2014/03/f8/deer12_greszler.pdf, accessed: 2014-08-07. URL http://energy.gov/sites/prod/files/2014/03/f8/deer12_greszler.pdf>.
[4] Leising C, Purohit G, DeGrey S, Finegold J. Waste heat recovery in truck engines. SAE technical paper 780686; 1978. http://dx.doi.org/10.4271/780686.
[5] Aly SE. Diesel engine waste-heat power cycle. Appl Energy 1988;29:179–89.
[6] Endo T, Kawajiri S, Kojima Y, Takahashi K, Baba T, Ibaraki S, et al. Study on maximizing exergy in automotive engines. In: Proceedings of the SAE 2007 world congress and exhibition; 2007. SAE technical paper 2007-01-0257. http://dx.doi.org/10.4271/2007-01-0257.
[7] Katsanos CO, Hountalas DT, Pariotis EG. Thermodynamic analysis of a Rankine cycle applied on a diesel truck engine using steam and organic medium. Energy Convers Manage 2012;60:68–76.
[8] Reck M, Randolf D. An organic Rankine cycle engine for a 25-passenger bus. SAE technical paper 730219; 1973. http://dx.doi.org/10.4271/730219.
[9] Kruiswyk RW. Air systems technologies for efficiency: heavy-duty off-road engine applications, keynote presentation. In: IMechE 2nd workshop on engine downsizing and turbocharging, Imperial College London; May 2014.
[10] Koeberlein D. Cummins SuperTruck program – technology and system level demonstration of highly efficient and clean, diesel powered class 8 trucks. DOE vehicle technologies office annual merit review presentation; May 2013. <http://energy.gov/sites/prod/files/2014/03/f13/ace057_koeberlein_2013_o.pdf [accessed 06.08.14].
[11] Quoilin S, Sart-tilman C. Expansion machine and fluid selection for the organic Rankine cycle. In: Proceedings of the 7th international conference on heat transfer, fluid mechanics and thermodynamics; 2010.
[12] Sprouse III C, Depcik C. Review of organic Rankine cycles for internal combustion engine exhaust waste heat recovery. Appl Therm Eng 2013;51:711–22.
[13] Quoilin S. Sustainable energy conversion through the use of organic Rankine cycles for waste heat recovery and solar applications. PhD thesis. University of Liége; October 2011.
[14] Bao J, Zhao L. A review of working fluid and expander selections for organic Rankine cycle. Renew Sust Energy Rev 2013;24:325–42. http://dx.doi.org/10.1016/j.rser.2013.03.040.

[15] Clemente S, Micheli D, Reini M, Taccani R. Bottoming organic Rankine cycle for a small scale gas turbine: a comparison of different solutions. Appl Energy 2013;106:355–64. http://dx.doi.org/10.1016/j.apenergy.2013.02.004.
[16] Uusitalo A, Colonna P, Larjola J, Honkatukia J, Turunen-Saaresti T. Siloxanes as working fluids for mini-ORC systems based on high-speed turbogenerator technology. Trans ASME J Eng Gas Turb Power 2013;135(4):042305-1–5-9. http://dx.doi.org/10.1115/1.4023115. paper no: GTP-12-1051.
[17] Macchi E. Design criteria for turbines operating with fluids having a low speed of sound in closed cycle gas turbines. Lecture series 100 on closed cycle gas turbines, von Karman Institute for Fluid Dynamics; 1977.
[18] Wheeler APS, Ong J. The role of dense gas dynamics on organic Rankine cycle turbine performance. Trans ASME J Eng Gas Turb Power 2013;135(10):102603-1–3-9. http://dx.doi.org/10.1115/1.4024963. paper no: GTP-13-1214.
[19] Liu B-T, Chien K-H, Wang C-CC-C. Effect of working fluids on organic Rankine cycle for waste heat recovery. Energy 2004;29(8):1207–17. http://dx.doi.org/10.1016/j.energy.2004.01.004.
[20] van Buijtenen JP. The Tri-O-Gen organic Rankine cycle: development and perspectives. Power Eng 2009;13(1):4–12.
[21] Quoilin S, Broek MVD, Declaye S, Dewallef P, Lemort V. Techno-economic survey of Organic Rankine Cycle (ORC) systems. Renew Sust Energy Rev 2013;22:168–86. http://dx.doi.org/10.1016/j.rser.2013.01.028.
[22] Fernández FJ, Prieto MM, Suárez I. Thermodynamic analysis of high-temperature regenerative organic Rankine cycles using siloxanes as working fluids. Energy 2011;36(8):5239–49.
[23] US Environmental Protection Agency. Office of pollution and toxics, chemicals in the environment: toluene, OPPT chemical fact sheet; August 1994. <http://www.epa.gov/chemfact/f_toluen.txt> [accessed 13.08.14].
[24] National Institute of Standards and Technology. NIST standard reference database 23, Web page; 2013. <http://www.nist.gov/srd/nist23.cfm> [accessed 20.10.13].
[25] Dixon SL. Fluid mechanics and thermodynamics of turbomachinery. 4th ed. Butterworth-Heinemann; 1998.
[26] Japikse D, Baines NC. Introduction to turbomachinery. 1st ed. Concepts ETI, Inc. and Oxford University Press; 1997.
[27] Fiaschi D, Manfrida G, Maraschiello F. Thermo-fluid dynamics preliminary design of turbo-expanders for ORC cycles. Appl Energy 2012;97:601–8. http://dx.doi.org/10.1016/j.apenergy.2012.02.033.
[28] Colonna P, Rebay S, Harinck J, Guardone A. Real-gas effects in ORC turbine flow simulations: influence of thermodynamic models on flow fields and performance parameters. In: Proceedings of the European conference on computational fluid dynamics (ECCOMAS CFD 2006); 2006. p. 1–18.
[29] Logan Jr E, Roy R, editors. Handbook of turbomachinery. CRC Press; 2003.
[30] Rodgers C, Geiser R. Performance of a high-efficiency radial/axial turbine. Trans ASME, J Turbomach 1987;109(2):151–4. http://dx.doi.org/10.1115/1.3262077.
[31] Whitfield A, Baines NC. Design of radial turbomachines. 1st ed. Longman Scientific & Technical; 1990.
[32] Hoshide RK, Nielson CE. Study of blade clearance effects on centrifugal pumps. Tech Rep CR-120815, NASA; 1972.
[33] Abidat M. Design and testing of a highly loaded mixed flow turbine. PhD thesis. Imperial College of Science, Technology and Medicine, University of London; 1991.